KEK_J-PARC-PAC2010-08

Updated Revised Proposal

Direct measurements of ω mass modification in A(π^-, n)ωX reaction and $\omega \to \pi^0\gamma$ decays

July 5, 2010

K. Ozawa[1], S. Masumoto, K. Utsunomiya, Y. Watanabe,
Y. Komatsu, A. Takagi and R.S. Hayano

Physics department, Graduate School of Science, University of Tokyo

S. Yokkaich, K. Aoki

RIKEN

Y. Morino

Research Center for Nuclear Physics, Osaka University

H. Shimizu, T. Ishikawa, H. Yamazaki

Research Center for Electron Photon Science, Tohoku University

T. Takahashi, J. Imazato

IPNS, KEK

[1]Contact person, e-mail:ozawa@phys.s.u-tokyo.ac.jp

Contents

1 Physics Goal

The origin of the hadron mass has been drawing strong interests in nuclear and particle physics. Especially in QCD, mass of hadrons is composed of a sum of the effective mass of valence quarks, known as constituent quark mass, and their interaction term. According to theoretical models, the effective mass of valence quarks is determined by chiral property of QCD vacuum. This mechanism is understood as a consequence of the dynamical breaking of chiral symmetry. In hot and/or dense matter, this broken symmetry will be restored either partially or completely and, hence, properties of hadrons, such as mass, decay modes and life time, can be modified. Therefore, we can study the origin of hadron mass and chiral properties of QCD medium by measuring in-medium properties of mesons. Especially, mass spectra of vector mesons is directly connected to anti-quark quark condensates [1], which is an order parameter of chiral symmetry. Relatively large mass modification is theoretically expected even at nuclear density [2]. Thus, we focus on ω meson mass in nucleus in this propose experiment.

Mass of ω meson at finite density, such as nucleus, has been studied in many theoretical methods. Hatsuda and Lee studied using a QCD sum rule and partial chiral symmetry restoration. They predicted 10$\sim$20% decreasing for ρ/ω mass at normal nuclear density [1]. Klingl *et al.* calculated the downward mass-shift and even mass broadening of $\rho/\omega/\phi$ in dense matter [3]. Some models considered couplings to baryon resonances and predicted broadening and slight increasing of ω mass [4, 5].

There are several theoretical activities, however, there is no conclusive result experimentally. The main purpose of the proposed experiment is measurements of direct ω mass modification under a clear condition. The proposed experiment focus on establishing the mass modification of ω meson using measurements of ω meson decays. Decays of ω meson in nucleus are measured with $\omega \to \pi^0\gamma$ mode in low momentum region, since slowly moving ω mesons can be expected to decay inside nucleus and have a large effect of mass modification. Such low momentum ω mesons can be generated in A(π^-, nω)X reaction using a kinematic matching. Following physics issues are studied in the proposed experiment.

- Nuclear transparency ratio and ωN interaction
- Mass modification in invariant mass measurements
- Nuclear bound state of ω meson

First, a nuclear transparency ratio of ω meson is measured using several target data as a base measurement. Measured atomic number dependence

of ω meson yield can be interpreted into the nuclear transparency ratio and cross section of ωN interactions. In this measurements, ω mesons decayed outside nucleus are needed and we can have enough statistics.

Next, we can discuss about details of invariant mass distribution of ω in $\pi^0\gamma$ invariant mass distribution. Modification of invariant mass can be searched using γ detector with a good resolution. To evaluate experimental effects due to a systematic bias by detectors, we will use Liquid Hydrogen target. Since we are performing specified measurements focused on low momentum region, expected mass modification will be large. However, the signal significance depends on the amount of mass shift and width broadening. If the width broadening of ω in nuclei is too large to measure invariant mass, we can obtain information about the width broadening using the atomic number dependence of ω cross section. Such approach is adopted in KEK-E325 experiment [6] and can give a strong limitation to a width broadening of ω in nucleus.

In addition, a combined measurement is performed to have a clear initial condition and an additional information about ωN interactions.. Initial conditions and decays of produced ω meson are measured in A(π^-, nω)X reaction. Fig.1 shows a schematic view of combined measurements. Using

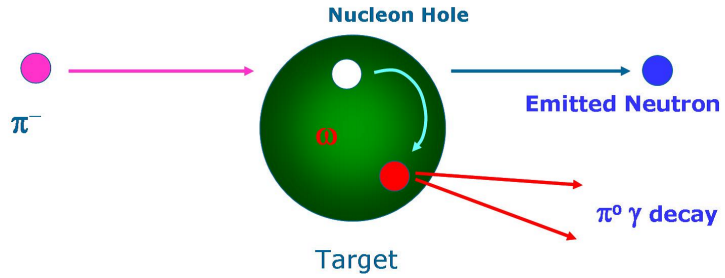

Figure 1: Schematic view of combined measurements

missing mass information in forward neutron measurements, the generation process of ω meson can be identified. In addition, ω meson is generated in recoil less kinematics and the momentum of generated ω meson is very limited within the Fermi motion. Also, if ω meson is bounded in nucleus, which can be observed using the forward neutron measurement, the kinematic condition of ω meson in nucleus is established very clearly.

Besides such physics advantages, there is an experimental advantage. Simultaneous measurements can reduce a combinatorial background strongly. Evaluation of combinatorial background is a major issue in the direct mass measurements via decays. M. Kaskulov *et al.* claims that TAPS results [7] are not robust under shape difference of combinatorial background [8]. In the

proposed experiment, combined measurements can achieve small background measurements.

Also, nuclear ω bound states can be searched in A(π^-, n)ωX reaction, if a strongly bounded ω state exists. This is the first measurement to see ω bound state in nucleus. Calculations about possible ω bound states have been developed by several groups. W. Weise and his group predict 30 MeV binding energy [9]. H. Nagahiro *et al.* predict 50 MeV binding energy using an optical potential method [8, 10]. Fig.2 shows a prediction of ω bound sate from [10].

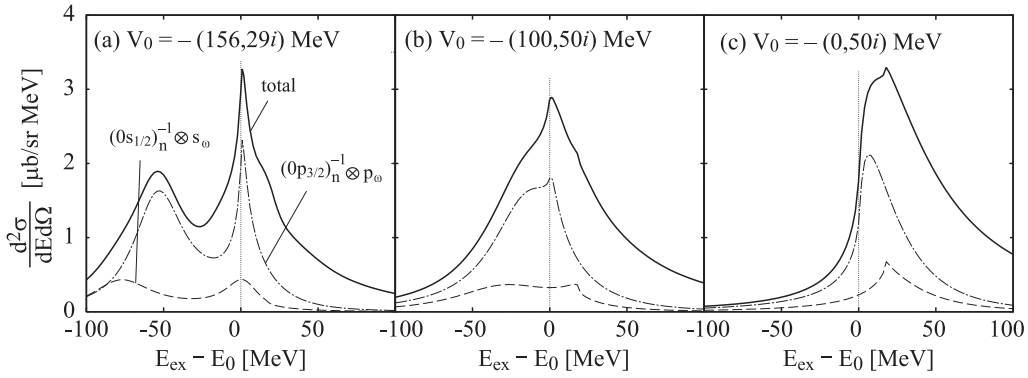

Figure 2: Calculated spectra of ^{12}C(π^+,p)^{11}C$\otimes\omega$ reaction as functions of the excited energy $E_{\rm ex}$. E_0 is the ω production threshold. The neutron-hole states are indicated as $(n\ell_j)_n^{-1}$ and the ω states as ℓ_ω [10].

When a binding energy of a ω bound state in nucleus is measured, it can be interpreted to an optical potential and gives a phenomenological information about interactions between ω meson and nuclei. If mass distribution of bounded ω meson is measured directly via decays, the relation between mass distribution and nuclear-meson interaction is established experimentally. Then, the amount of ω mass shift in direct mass spectrum and ω binding energy can be compared. Such comparison gives information about effects beyond the meson nuclei interaction, such as chiral symmetry restoration. Using established experimental relation, there is a possibility to understand ωN interaction within a frame work of Quantum Chromo Dynamics.

2 Existing experimental results

There is no conclusive experimental results at this moment for ω meson. Some experiments have been performed to measure mass modification of other vector mesons.

The KEK-PS E325 experiment [11] measured the e^+e^- decays of light vector mesons ($\rho/\omega/\phi$) made by the 12–GeV proton induced reaction in target nucleus. Their results show 9% decreasing of ρ meson mass. It can be expected that ω meson has the same mass decreasing as ρ, since both mesons have the same quark contents. However, ω peak is sitting on ρ's broad peak and the measurement has small sensitivities for ω meson mass modification.

Recently, CLAS at J-Lab reported mass broadening of ρ meson in γA reactions, though they did not observe mass decreasing [12]. They have small sensitivities for ω meson mass modification due to the same reason as the KEK experiment.

As a comparison between two experiments, it should be noted that the initial condition of generated ω meson is important, since the difference between CLAS and KEK results can be understood as the difference of production process. Thus, the initial condition of ω meson need to be determined simultaneously and the current proposed experiment will give such measurements.

Mass spectral of ω meson in nucleus were measured by the CBELSA / TAPS experiment in $\pi^0\gamma$ decay channel in γA reactions [7]. Since ρ mesons have a very small branching ratio (6.0×10^{-4}) to $\pi^0\gamma$ decays, contribution of ρ meson is negligible in this measurement. Originally, they claims 14% decreasing of ω mass [7]. However, obtained spectra are slightly changed [13] as shown in Fig.3 and there is no evidence for mass modification at this moment. Updated mass shape for Nb target is consistent with one for LH_2 target. Momentum range of ω mesons measured by TAPS is too high to detect mass modification.

To detect mass modification of ω meson in nuclei, we need to measure mass spectra of ω mesons decayed inside nuclei. The fraction of mesons decayed inside nucleus strongly depends on their momentum and decay width in nucleus. K. Gallmeister *et al.* calculated mass spectra of ω meson for TAPS experiment with and without mass modification using Gi-BUU transport model [15]. As a results, there is very small difference between those spectra, since very small fraction of generated ω meson decayed into $\pi^0\gamma$ inside nucleus.

What we have learn from TAPS results is that ω mesons with small momentum need to be detected and effects of decay width in nucleus need to be carefully taken into account for yield evaluation. For the first point, we focus on almost stopped ω mesons (less than 50 MeV/c). This condition is

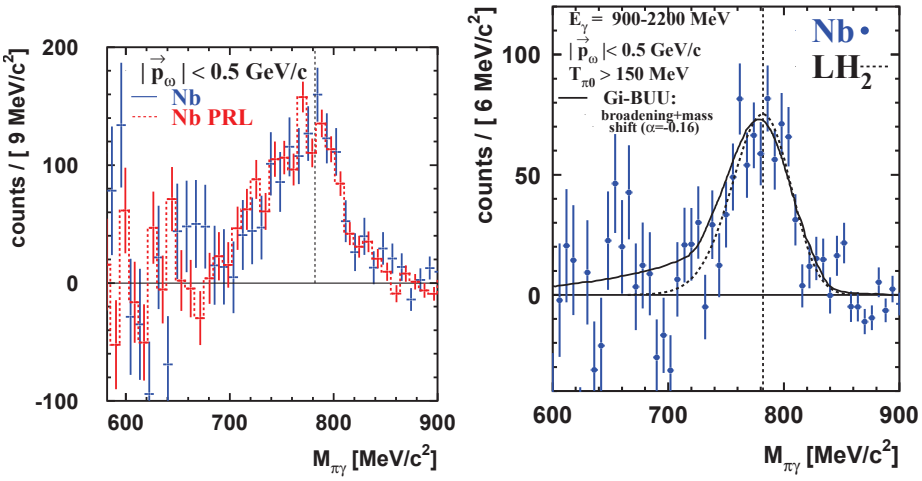

Figure 3: (Right Figure) ω signal for the Nb target from updated analysis [13] (solid points) compared to the ω signal published in [7] (dashed). (Left Figure)ω signal for the Nb target in comparison to the ω line shape measured on a LH_2 target (dashed curve) and GiBUU simulation [14] (solid curve).

achieved by combined measurements of forward neutron and ω meson decays.

Another issue is large width of ω meson in nucleus. The TAPS group reported larger decay width in nucleus due to interactions between ω mesons and nucleus [16]. As shown in Fig.4, based on measured transparency factor by TAPS experiment, total width of ω meson in the nuclear medium is evaluated. The calculation need to be extrapolated to lower momentum region, since our target momentum region is less than 50 MeV/c and TAPS does not cover the lower momentum region. Normalized BUU calculation (red line) is used for the extrapolation. The BUU calculation takes into account known hadronic interactions and uses ωN interaction cross section measured by TAPS as input. As shown in Fig.4, the width of 60 MeV/c^2 can be applied for the momentum region of less than 50 MeV/c. Thus, the branching ratio of $\pi^0\gamma$ decays in nucleus becomes 1.5% of total decays instead of 8.92% in free space.

As shown in Fig.2, assumed potential in the calculation of H. Nagahiro *et al.* is consistent with the TAPS and BUU evaluation. H. Nagahiro *et al.* assumed 29 MeV/c^2 for imaginary part of the potential and it corresponds to the width of 58 MeV/c^2. The calculation of H. Nagahiro *et al.* is for generation of ω meson and takes into account several nuclei effects. Thus, we estimate our final yield based on their calculation. Details of our estimation are described later.

Calculations for extracting the in-medium width from TAPS data is based

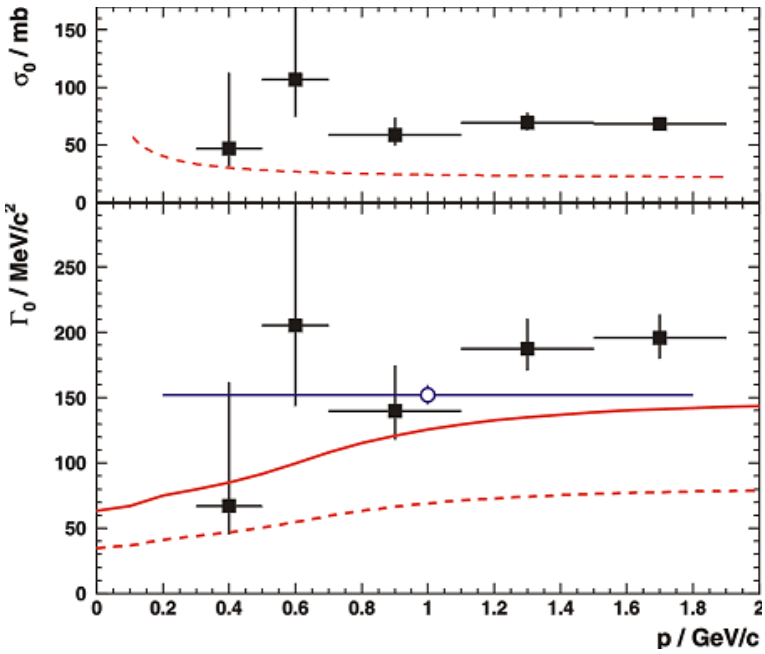

Figure 4: Figure and caption are taken from [16]. Upper part: The inelastic ωN cross section extracted from the Glauber analysis (data) in comparison to the inelastic cross section used in the BUU simulation [14]. Lower part: Width of the ω meson in the nuclear medium in the nuclear rest frame as a function of the ω momentum in a Glauber analysis (squares), from the Giessen BUU model with the inelastic cross section from the upper figure (red dashed line), and after fit to the TAPS data with BUU [solid gray (red) line], and the Valencia Monte Carlo simulation (blue circle), respectively.

on the transparency ratio, defined as

$$T = \frac{\sigma_{\gamma A \to VX}}{A\sigma_{\gamma N \to VX}} \tag{1}$$

i.e. the ratio of the inclusive nuclear ω photo-production cross section divided by A times the same quantity on a free nucleon. T describes the loss of flux of ω mesons in nuclei and is related to the absorptive part of the ω nucleus potential and thus to the ω inelastic width in the nuclear medium.

In the current proposed experiment, measurement of ω production cross section and the transparency ratio is important to extract ω inelastic width in the nuclear medium. Especially, effects of mass modification becomes large in low momentum region, since large fraction of low momentum ω is decayed inside nuclei. Thus, it is important to measure ω in low momentum region and it is not measured by the TAPS experiment.

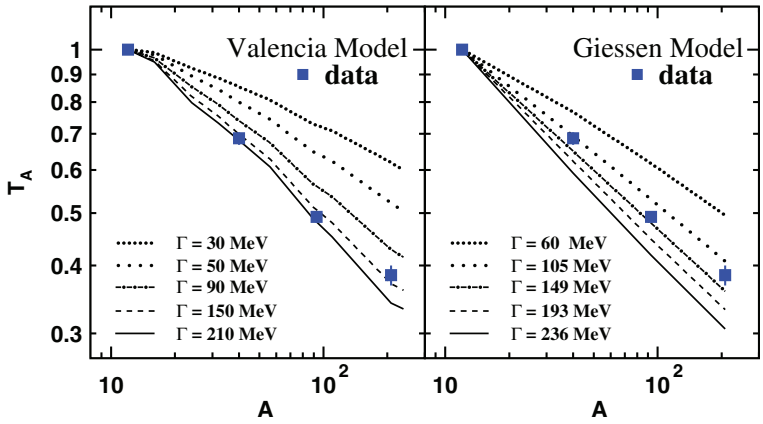

Figure 5: Figure and caption are taken from [16]. Experimentally determined transparency ratio, defined as $T_A = \frac{12\sigma_{\gamma A \to VX}}{A\sigma_{\gamma C_{12} \to VX}}$, in comparison with a theoretical Monte Carlo simulation [17] and a BUU calculation [14].

3 Experimental Apparatus

The main purpose of the proposed experiment is establishing the mass modification of ω meson using measurements of ω meson decays. Also, the proposed experiment aims measurements of direct ω mass modification under a clear condition. We have following measurements in the current proposal to achieve our physics goal.

- Atomic Number Dependence of ω production cross section
- Invariant mass measurements for several targets in low momentum region
- Nuclear bound state of ω meson
- Combined measurements with invariant mass and missing mass measurements

All measurements can be done at the same time, however, we need to have a specified trigger for each measurement.

We measured A(π^-, n)ω reaction with forward neutron measurements and decays of generated ω meson with $\omega \to \pi^0\gamma$ mode and π^0 meson is detected with 2 γ decays. In the measurements, two detectors are needed. One is gamma-ray detector for detecting 3 γ's at target region and another is neutron counter at the forward region. To measure nuclear target dependence, we have following targets, such as Liquid-Hydrogen, Carbon, Calcium, and Niobium. The beam momentum of 1.8 GeV is chosen to have recoil less production of ω meson. To achieve the required beam momentum, K1.8 beam line needs to be used. The beam intensity of 10^7 per spill is also required to collect reasonable amount of yield, as described later. Momentum of incident π^- beam is measured by tracking devices at the beam line. The resolution of missing mass measurements is mainly determined by the resolution of forward neutron momentum measurements and the required resolution for π^- momentum is about 1%.

We measure decays of ω meson using $\omega \to \pi^0\gamma$ mode and π^0 meson is detected with 2 γ decays. Thus, total 3 γ's need to be detected. We focus on relatively low momentum ω mesons and and decayed γ and π^0 goes to back to back. Thus, large acceptance is needed to the γ detection. We have two options about gamma-ray detector. One is the gamma-ray detector used for KEK E246 experiment and another candidate is newly constructed detector at Tohoku University.

The E246 detector has 75% acceptance and consists of CsI crystals. The detector has 12 large holes and we are planning to fill the "holes" and the

acceptance will be 94%. We submitted a grant to obtain additional crystals. The read out of the detector will be upgraded for a new T-violation experiment (E06) at J-PARC. Another candidate of gamma-ray detector is made by Tohoku University and consists of BGO crystals. It's under the construction and preliminary R&D shows a similar energy resolution with the E246 detector. Details of the gamma-ray detector and simulation results are described later.

In addition, incident π^- meson and forward neutron in A(π^-, n)X reaction are measured and missing mass is calculated to identify ω meson production. The forward neutron momentum is measured using newly constructed neutron counter and time of flight method. Emitted neutron should be detected at 0 degree to minimize momentum transfer to ω meson. Produced charged particles as a background and π^- beam are swept by a magnet. The SKS magnet can be used for such sweeping. Details of neutron detector are described later.

3.1 Target

We have several targets to measure atomic number dependence of ω production cross section and invariant mass distribution. Target thickness and required shifts are shown in Table 1.

Table 1: Target configuration

Target	Thickness [cm]	Required shifts	comments
For Atomic number dependence			
Liquid Hydrogen	6	30	
Carbon	6	30	
Calcium	6	30	
Niobium	0.3	100	Thin to avoid Radiation loss
For combined measurements			
Carbon	6	90	In addition to above shifts

A liquid hydrogen target as a proton target is important to check our experimental effects and clearly demonstrate the modifications of ω mass in nuclei.

The carbon target is suitable both for the bound state search and invariant mass measurements in nucleus. We can clearly identify the ω bound state and enough size to detect the mass modification of ω, when low momentum ω is selected.

Heavy nucleus targets, such as Calcium, and Niobium, are suitable for measurements of ω meson mass modification, since a possibility of ω decaying inside nucleus becomes larger using larger nuclei. In addition, we can extract ωN interaction cross section in nucleus from production cross sections of ω mesons and its target dependence. However, the bound state search becomes difficult, since there are many nucleon states and it's hard to identify ω bound state.

4 Gamma-ray detector and simulation study

As shown in the previous proposal, we developed a fast simulation code to evaluate a realistic mass resolution of a gamma-ray detector. An energy resolution, an angular resolution and a shower leak at a crystal have been considered on the code. At first, the code is tuned to reproduce existing experiment data. Then, we simulate for ω meson mass reconstruction using this code.

We have another candidate for the gamma detector which is constructed at Tohoku University. The characteristics of new detector is briefly summarized in the last of this section.

4.1 Existing data

Existing experiment data are obtained from stopped kaon decay [18, 19]. These data are shown in Fig.6 to Fig.8, and obtained resolutions are in the caption of figures and summarized in Table 2.

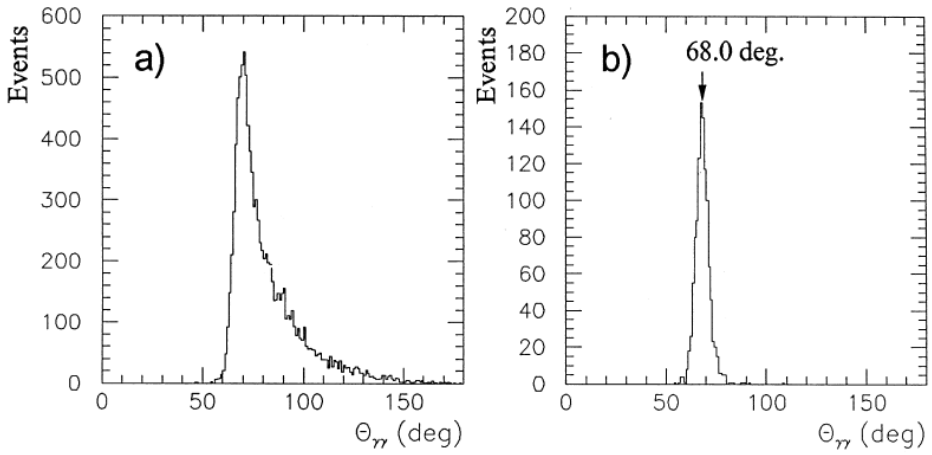

Figure 6: Measured distribution of an opening angle between two photons from π^0 in $K^+ \to \pi^+\pi^0$ decays: (a) all $K^+ \to \pi^+\pi^0$ events are shown; (b) events with $(E_1 - E_2)/(E_1 + E_2) \leq 0.1$ are presented. The minimum opening angle of 68.03 is obtained.

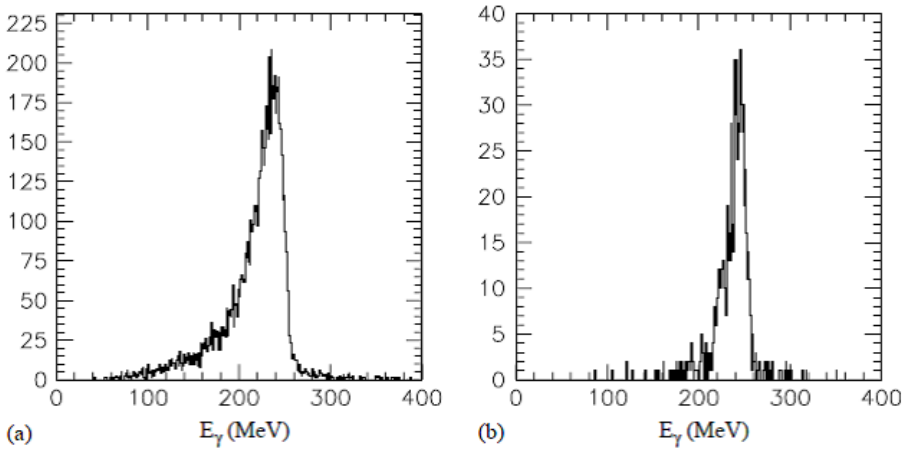

Figure 7: Energy sum of two photons from the π^0 in $K^+ \to \pi^+\pi^0$ decays. (a) All events with peak value $E_{\gamma\gamma} = 235.7$MeV, $\sigma = 5.2\%$. The low energy tail is due to the shower leakage into muon and beam holes. (b) Photons are detected away from muon holes. $E_{\gamma\gamma} = 242.5$MeV, $\sigma = 4.1\%$.

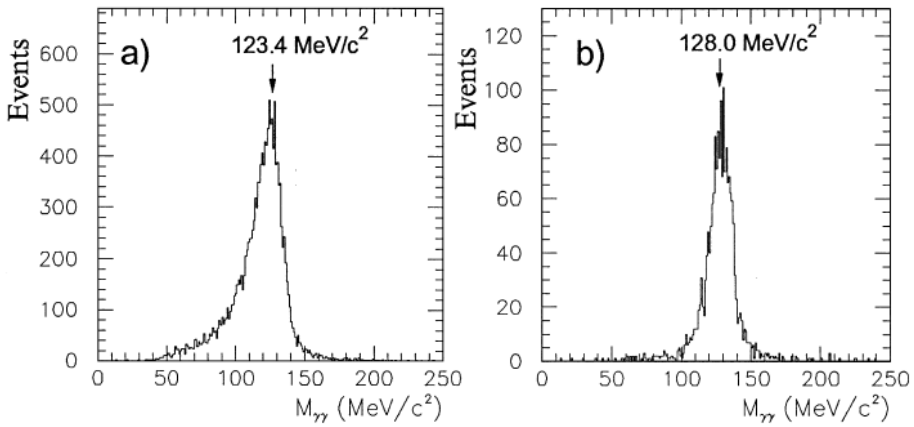

Figure 8: Invariant mass of $\gamma - \gamma$ events from $K^+ \to \pi^+\pi^0$ decays; (a) all events reconstructed in the π^0 detector; (b) events detected away from the muon holes area.

4.2 Simulation tuning

In the reference data, a stopped K^+ decays into π^0 and π^+, and the π^0 also decays into 2 γ's. On our simulation, the reaction is simulated and γ's are

detected by the gamma-ray detector. The geometry of gamma-ray detector is shown in Fig.9. The detector is used for KEK E246 experiment. An energy resolution, an angular resolution and shower leaks at crystals are tuned to fit the existing data. As a base characteristics of the detector, the gamma-ray detector has the 4.3% energy resolution σ_E/E at 100 MeV and 2.8% at 200 MeV [18]. We assume that the energy resolution can be understood as a quadratic sum of energy dependent part and constant part, and the function of the energy resolution is shown in Fig.10. The mark, $\oplus$, represents addition in quadrature: $\frac{\sigma_E}{E} = \frac{a}{\sqrt{E}} \oplus \frac{b}{E}$ represents $\left(\frac{\sigma_E}{E}\right)^2 = \left(\frac{a}{\sqrt{E}}\right)^2 + \left(\frac{b}{E}\right)^2$

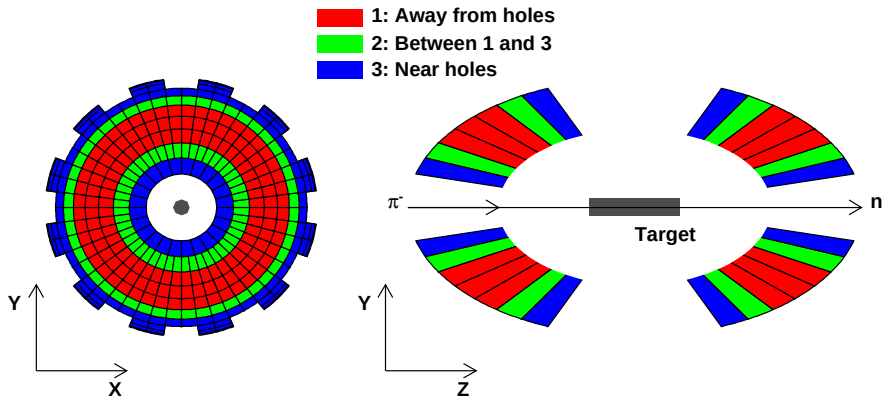

Figure 9: Schematic view of gamma-ray detector. Red parts and blue parts are the crystals which away from holes and near the holes respectively. Green parts are the crystals between red and blue parts.

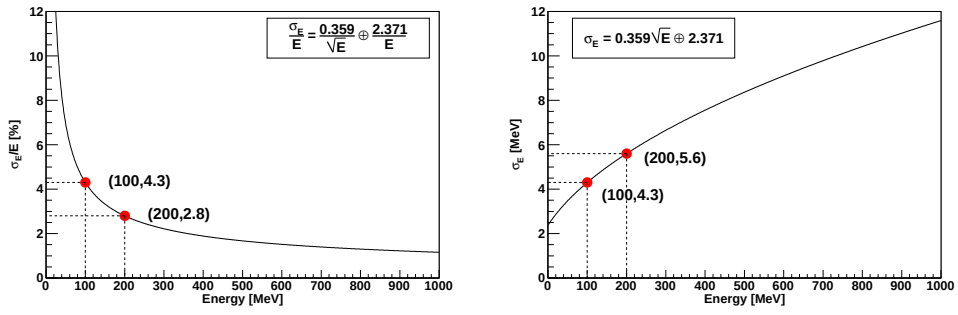

Figure 10: Assumed energy resolution function of gamma-ray detector. $\oplus$ represents addition in quadrature.

To evaluate shower leak effects of the detector, the leak effects of γ's are

parameterized as shown in Fig.11 and Fig.12. Fig.11 shows the effects of longitudinal leaks. Light absorption values are described as an electromagnetic cascade, like,

$$\begin{aligned} \text{Light absorption} &= \frac{1}{E_0}\int_0^t \frac{dE}{dt}dt \\ &= \frac{1}{E_0}\int_0^t b\frac{(bt)^{a-1}e^{-bt}}{\Gamma(a)}dt, \end{aligned} \tag{2}$$

here,

$$\begin{aligned} &t = x/X_0 = \text{depth in radiation lengths}, \\ &b \approx 0.5, \\ &a = b(\ln y + 0.5) + 1, \\ &y = E_\gamma/E_c. \end{aligned}$$

x is length of crystal, X_0 is radiation length: 1.85 cm for CsI(Tl) crystals, E_c is critical energy for electrons: 11.17 MeV and E_γ is induced photon energy.

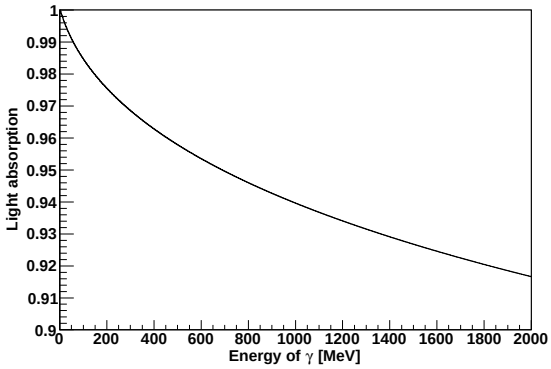

Figure 11: Longitudinal leaks as function of E_γ [MeV].

In addition to the longitudinal leaks, there are additional energy smearing and horizontal leaks as shown in Fig.12. A Gaussian is used for the γ's which has only longitudinal leaks and additional smearing, and a landau distribution for the γ's which hit near holes and have horizontal leaks. Additional smearing effect is caused by calibration issues and tuned to fit existing data.

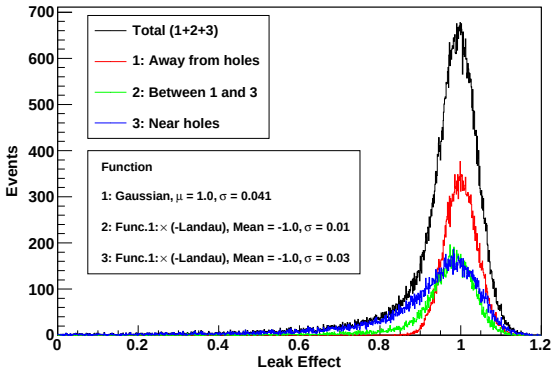

Figure 12: Effect of shower leak at crystals. Red, blue and green color are linked the colors in Fig.9.

Simulation histograms are shown in Fig.13 to Fig.15, and obtained results are summarized in Table 2.

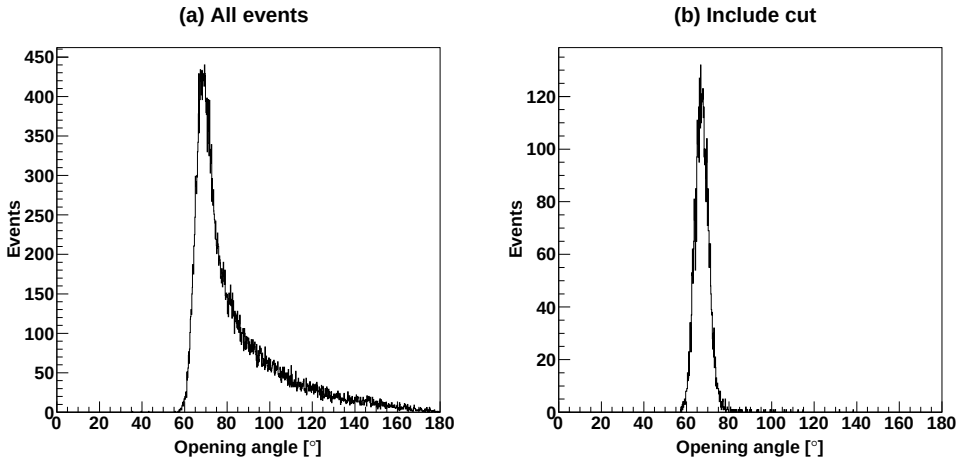

Figure 13: Simulated distribution of an opening angle between two photons from π^0 in $K^+ \to \pi^+\pi^0$ decays. All $K^+ \to \pi^+\pi^0$ events are shown in (a). Events with $-0.1 \leq (E_1 - E_2)/(E_1 + E_2) \leq 0.1$ are presented in a (b). The minimum opening angle of 67.1 is obtained.

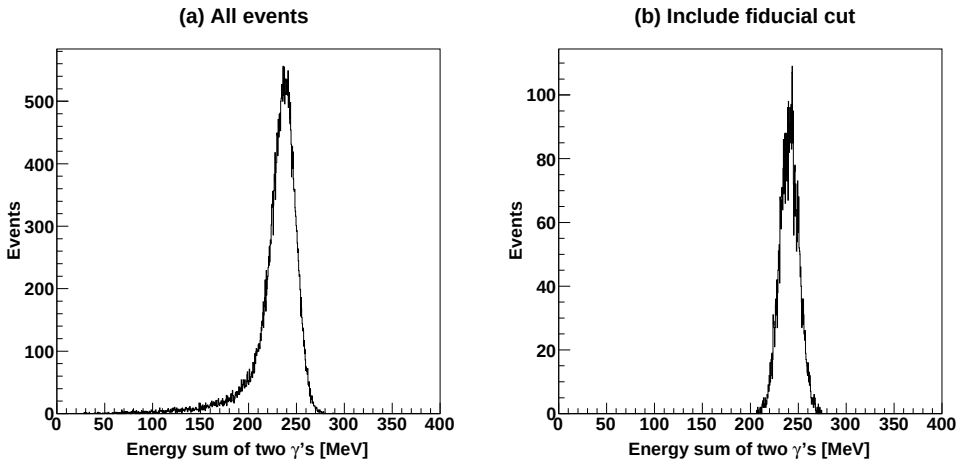

Figure 14: Simulated energy sum of two photons from the π^0 in $K^+ \to \pi^+\pi^0$ decays. All events with peak value $E_{\gamma\gamma} = 236.1$MeV, $\sigma = 5.2\%$ are shown in (a). The low energy tail is reproduced as Fig.7. (b) Photons are detected away from muon holes (fiducial cut, see section4.3). $E_{\gamma\gamma} = 240.5$MeV, $\sigma = 4.0\%$.

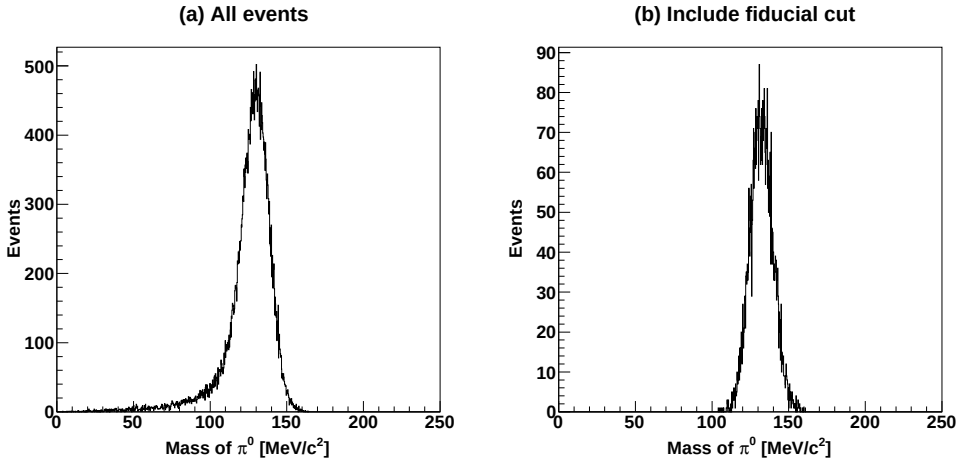

Figure 15: Simulated invariant mass of π^0 from $K^+ \to \pi^+\pi^0$ decays. All events with $m_{\pi^0} = 129.2\text{MeV/c}^2$ and $\sigma = 7.0\%$ are shown in (a). Events detected away from the muon holes area are shown in (b). $m_{\pi^0} = 132.5\text{MeV/c}^2$, $\sigma = 5.6\%$

Table 2: Summary of existing data and simulation

	Existing data	Simulation
The minimum opening angle [°]	68.03 [18]	67.1
Energy sum of two photons		
Peak value of all events [MeV]	235.7 [19]	236.1
σ[%]	5.2 [19]	5.2
Peak value of away from holes [MeV]	242.5 [19]	240.5
σ[%]	4.1 [19]	4.0
Invariant mass of π^0		
Peak value of all events [MeV/c^2]	123.4 [18]	129.1
σ[%]	6.7 [19]	7.0
Peak value of away from holes [MeV/c^2]	128.0 [18]	132.5
σ[%]	5.6 [19]	5.6

As shown in Table 2, our simulation is in excellent agreement with existing data.

4.3 Additional crystals for Muon holes

As shown in Fig.14 and Fig.15, a large tail is observed for γ's hit near holes. This tail can be a serious background of our measurements. Thus, we decided to have additional crystals to fill the muon holes. Then, all crystals except for two crystals both in forward and backward region have the same resolution as the red crystal in Fig.9. For γ's from π^0 decays, all crystals are used for detection.

4.4 Invariant mass evaluation

Invariant mass spectra of ω meson are simulated. Results are shown in Fig.16. A good mass resolution can be achieved. In this calculation, the muon holes of the gamma-ray detector are covered with CsI(Tl) crystals. Note: the gamma-ray detector still has beam holes, events of blue and green parts around beam hole are cut as a fiducial cut.

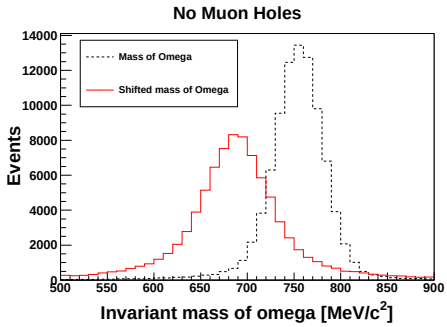

Figure 16: Invariant mass of ω meson with gamma-ray detector which has no muon holes. Two lines represent ω mass shift = 0 (dotted line), 9% (red solid line).

4.5 Detector acceptance

The gamma-ray detector has a barrel structure that covers about 96.6% of 4π, when muon holes are covered by additional crystals. According to our simulation, the acceptance of ω decays is 89.3%. After applying the fiducial cuts, 82.7% of ω mesons are survived.

In addition, 1.2% of 2 γ's showers are merged and not distinguishable. It should be taken into account as an additional loss.

Table 3: Summary of the detector acceptance

	No muon holes
Geometry	96.6%
ω event	89.3%
Fiducial cut	82.7%
2γ merging	1.2%

4.6 Another candidate of Gamma detector

Prof. H. Shimizu and Dr. T. Ishikawa are developing a new γ detector at Tohoku University. The detector also has large acceptance (91% of 4π) and a good energy resolution as shown in Fig. 17. We are considering about using this detector for our experiment.

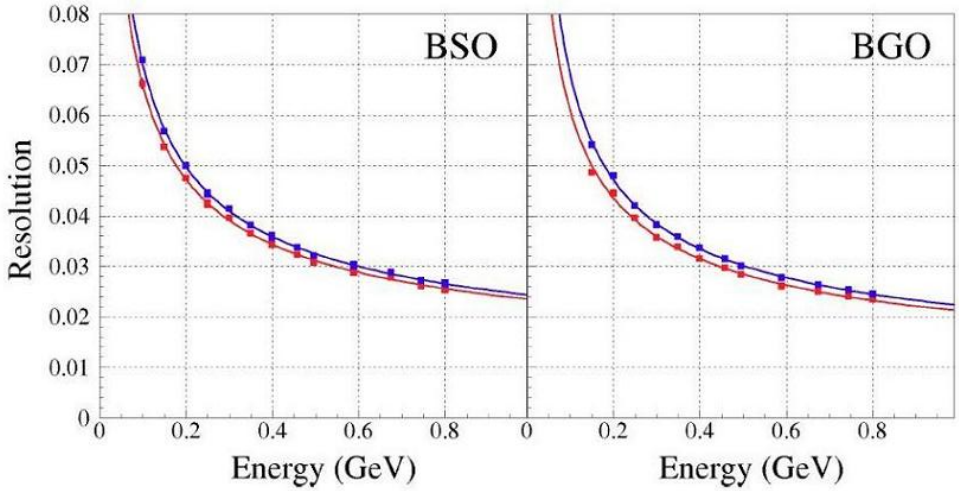

Figure 17: Energy resolution tested by Tohoku group for BSO and BGO crystals [20]. Blue points represent test results. Effects of beam energy spread is subtracted (red points).

The obtained result is similar with realistic E246 detector as shown in Table 2.

5 Neutron counter

Our neutron counter has 100mm× 30mm×600mm scintillators and the acceptance is about ±2°. A schematic view of neutron counter is shown in Fig.18. Momentum transfers as a function of the incident π^- momentum in the p(π^-,n)ω reaction are shown in Fig.19. To see a bound state, small momentum transfer is essential and neutron measurements are focused one the forward region. Also, we will have a specified trigger to find a bound state (see section 9). With the trigger, large statistics can be collected.

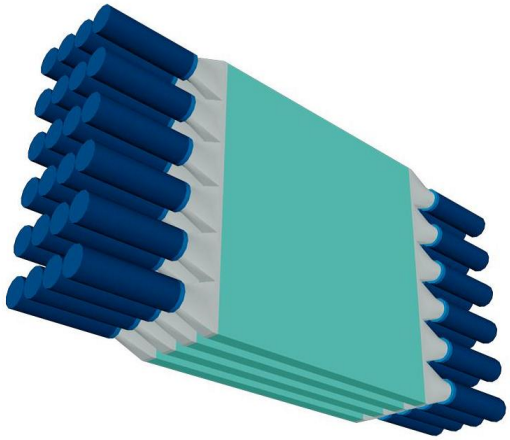

Figure 18: Schematic view of neutron counter.

5.1 Timing Resolution

According to calculation of H. Nagahiro *et al.* , shown in 2, mass resolution of 30MeV is needed to see a bound region, even when ω meson is strongly bounded. The mass resolution of 30MeV corresponds to 80ps of time resolution. When the neutron detection information is used to limit the ω momentum range and suppress the background, 30MeV of mass resolution is enough.

We performed a beam test at LNS GeV-γ beam line (Tohoku University) for a 100mm×30mm×600mm BC408 scintillator to see performance of the large scintillator matches our requirements. As a result, 56ps of time resolution is obtained, as shown in Fig.20.

A time lag between both ends of PMTs is shown in Fig.21. Three incident points on the scintillator were measured: center, 10cm shifted from the center and 20cm shifted from the center. A position resolution is decreasing as a

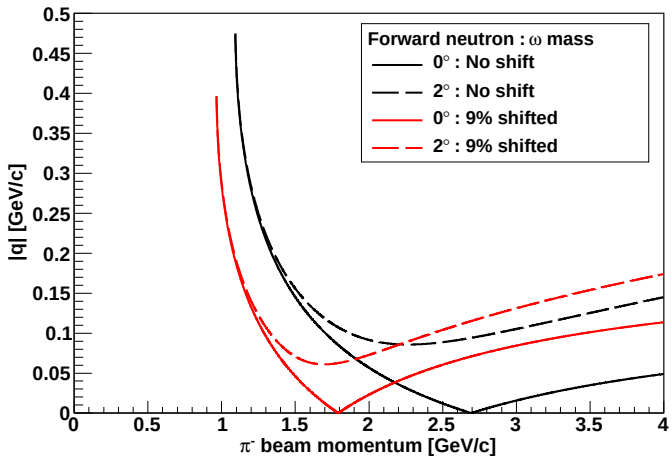

Figure 19: Momentum transfers as a function of the incident π^- momentum in the p(π^-,n)ω. The solid and dashed lines show the momentum transfers with forward neutron detection angle 0° and 2° respectively. The red lines indicate when the ω mass shifts 9%.

particle incidents near the edges of scintillator. However, this effect does not affect to the time resolution after slewing corrections with charge information.

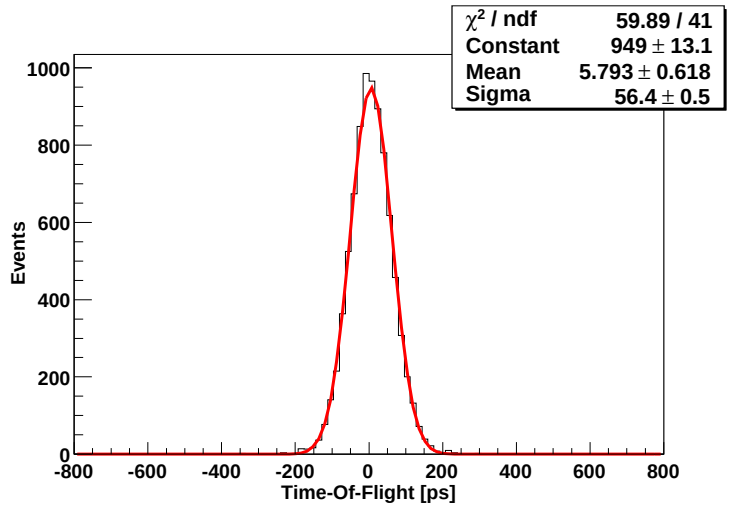

Figure 20: A spectrum of time-of-flight (TOF) at LNS beam test. 56ps time resolution is achieved as a result. It is enough for 80ps time resolution of required performance.

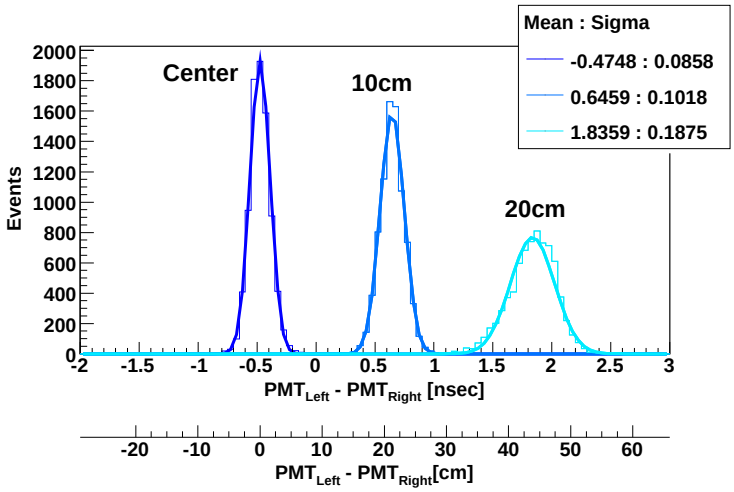

Figure 21: Histograms of position resolution for a 100mm×30mm×600mm scintillator. It indicates that the position resolution decreases as a particle incidents near the edges of scintillator. Difference of light propagation length between left and right PMT is shown under the horizontal axis. The light propagation length calculated with a light velocity and a refractive index of the scintillator.

5.2 Neutron detection efficiency

A Monte Carlo simulation used FLUKA package is done for evaluation of a neutron detection efficiency of the counter. Energy distributions of produced particles by neutron from the iron plates of 10mm thickness by neutron are shown in Fig.22.

Particle emission probabilities are summarized in Table 4. When all emitted protons are detected with the scintillators, 23.3% of neutron efficiency is achieved using 4 layers. Scintillator's own efficiency of 2.5% with 4 layers is also included.

A schematic view of cross section of the neutron counter with iron plates is shown in Fig.23.

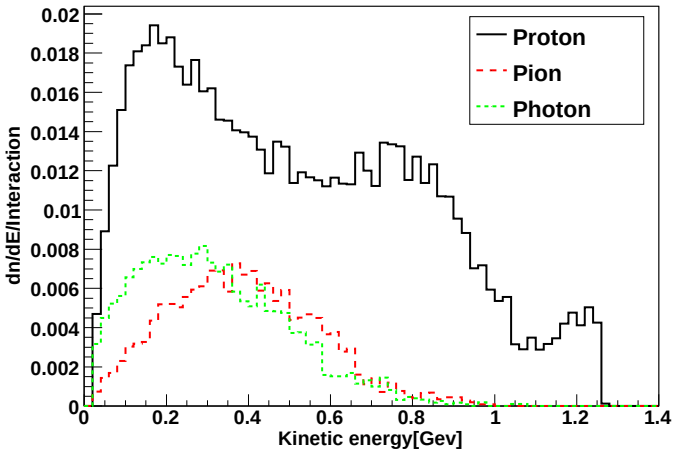

Figure 22: Energy distributions of produced particles from the iron plate 10mm thick by neutron.

Table 4: Particle emission probabilities

Protons per one neutron	5.2 %
Pions per one neutron	1.2 %
Photons per one neutron	2.1 %

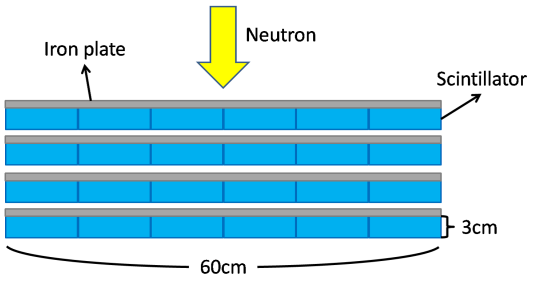

Figure 23: Schematic view of cross section of the neutron counter.

6 Yield and mass spectrum

We evaluate expected yield from a theoretical calculation based on measured cross sections. Then, expected invariant mass spectra and expected missing mass spectra are shown.

6.1 Base calculation

Obtained ω yield is estimated with measured cross section in p(π^-,n)ω reaction [21]. Fig.24 shows a summary plot of cross sections of backward ω production as function of $cos\theta_\omega$ [22]. H. Nagahiro *et al.* calculated the generation of ω and missing energy distribution based on the above experimental cross section and known nuclear effects as shown in Fig.2. In fact, the calculation is required forward neutron, however, we don't require the forward neutron and limit the momentum range of ω. The kinematic limitation of momentum range has the same effect as the detection of forward neutrons, the calculation is still valid for yield estimations. To obtained decayed spectra and yield, we have applied a branching ratio to $\pi^0\gamma$ decays empirically based on TAPS results. The calculation is done for ^{12}C and extrapolated to heavier targets. In the extrapolation, we assumed $A^{2/3}$ dependence of ω cross section. In fact, A-dependence of ω decayed inside nuclei is not known, however, such events can be occurred whole nuclear volume and $A^{2/3}$ dependence is conservative assumption.

The calculated spectrum is decomposed to two parts, such as conversion part and escape part, as shown in Fig.25. The calculation is done with a ^{12}C target and an attractive potential $V_\omega(r)$. Three kinds of potential are assumed as follows,

$$\text{(a) Figure 25 Top: } V_\omega(r) = -(156 + 29i)\frac{\rho(r)}{\rho_0} \ , \tag{3}$$

$$\text{(b) Figure 25 Middle: } V_\omega(r) = -(100 + 50i)\frac{\rho(r)}{\rho_0} \ , \tag{4}$$

$$\text{(c) Figure 25 Bottom: } V_\omega(r) = -50i\frac{\rho(r)}{\rho_0} \ . \tag{5}$$

The imaginary part of potential (a) is consistent with existing TAPS result [16] and the most feasible potential. The ω meson interacted with nuclei is presented as a conversion (green line). The ω meson which does not interacted with nuclei and escaped from nuclei is presented as an ω escape part (blue line). As described before, green line has a large width and only small fraction (1.5%) of ω decays into $\pi^0\gamma$. The total events are shown in a red line. An incident pion momentum of 1.8GeV/c is used in the calculation.

Based on the calculation, the expected yield and mass spectra are evaluated including several experimental effects.

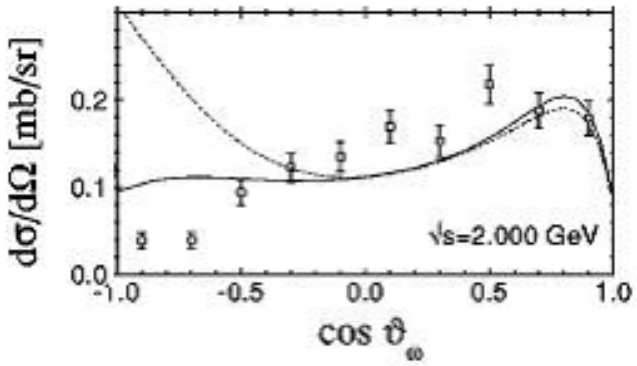

Figure 24: Summary plot of differential cross section of ω production as function of $cos\theta_\omega$ [22]. Points represent measurements. Lines represent theoretical calculations.

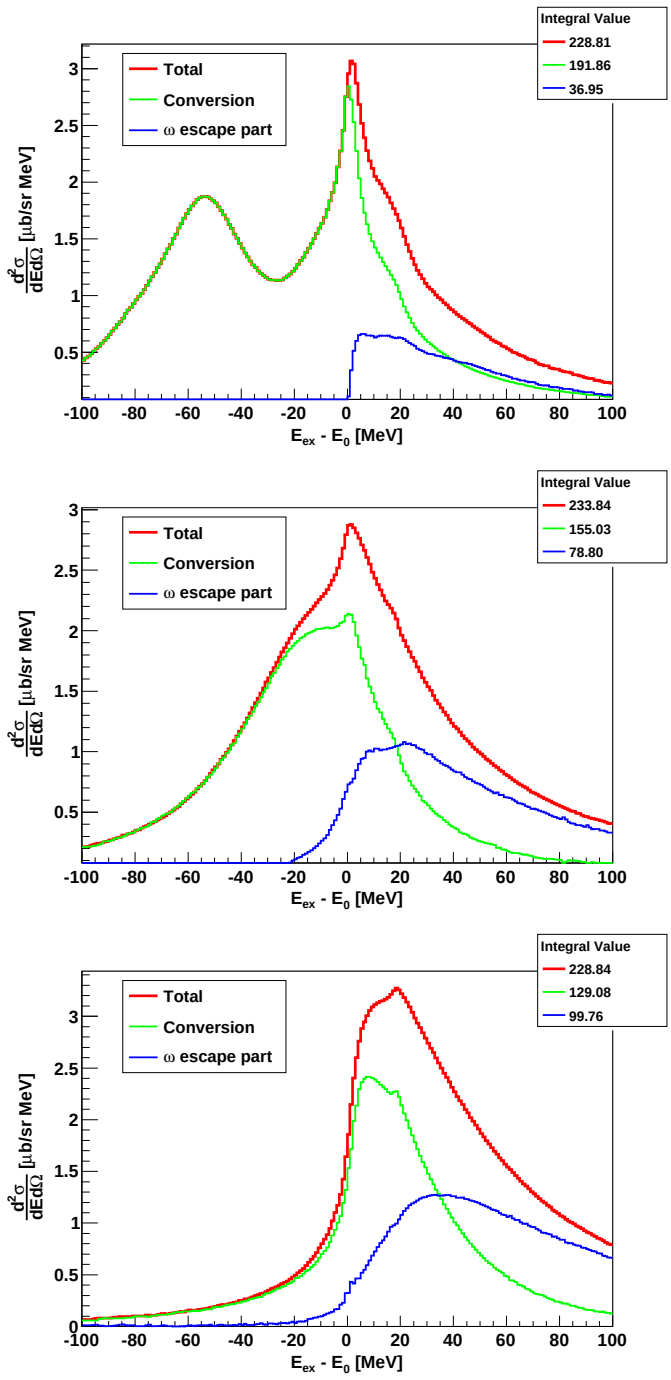

Figure 25: Calculated spectra of ^{12}C(π^+,p)^{11}C$\otimes\omega$ reaction cross section as functions of the excited energy E_{ex} [10]. An incident pion momentum is 1.8GeV/c. E_0 is the stopped ω energy; 782MeV.

6.2 Yield calculation

For yield calculation, we use an eq.(6) and parameters summarized in Table 5. Note: Detection of forward neutrons is note required in this measurements, however, effective acceptance of forward neutron is assumed in the calculation to evaluate a production cross section in the low momentum range.

$$Y = \frac{d^2\sigma}{dEd\Omega} \times BtoS \times I \times t\frac{\rho}{A}N_A \times AFN \times RLT \times FSI \times SPS \times BR \times E3G \times TRG \quad (6)$$

Y : Yield [/MeV 30shifts]

$\frac{d^2\sigma}{dEd\Omega}$: [μb/sr MeV] as shown in Fig.25

Table 5: Parameters of yield calculation eq.(6)

Parameter	Value	
$BtoS$	10^{-30}	μb $\rightarrow$ cm^2
I	10^7	Beam intensity [/Spill]
t	6	Target thickness [cm]
ρ	2.267	Target density (Carbon) [g/cm^3]
A	12.01	Atomic weight (Carbon) [g/mol]
N_A	6.022×10^{23}	Avogadro constant [/mol]
AFN	3.828×10^{-3}	effective Acceptance of Forward Neutron
		when low momentum ω is generated [sr]
RLT	0.89	Due to radiation loss in target (11%)
FSI	0.6	Without final state interaction
SPS	144000	Spills per 30 shifts
BR	-	Branching ratio $\omega \rightarrow \pi^0\gamma$
	0.089	for at free space (blue line in Fig.25)
	0.015	for inside nuclear (green line in Fig.25)
$E3G$	0.83	Acceptance of 3 γ's events
TRG	0.86	Trigger efficiency $\times$ Trigger Live Time

6.3 Expected invariant mass spectrum

An expected invariant mass spectrum is calculated and shown in Fig.26. We assume that the conversion part (green line in Fig.25) has 9% decreased ω

mass and the omega escape part (blue line in Fig.25) has no shifted ω mass. The expected mass spectra are shown in Fig.26 as a red line.

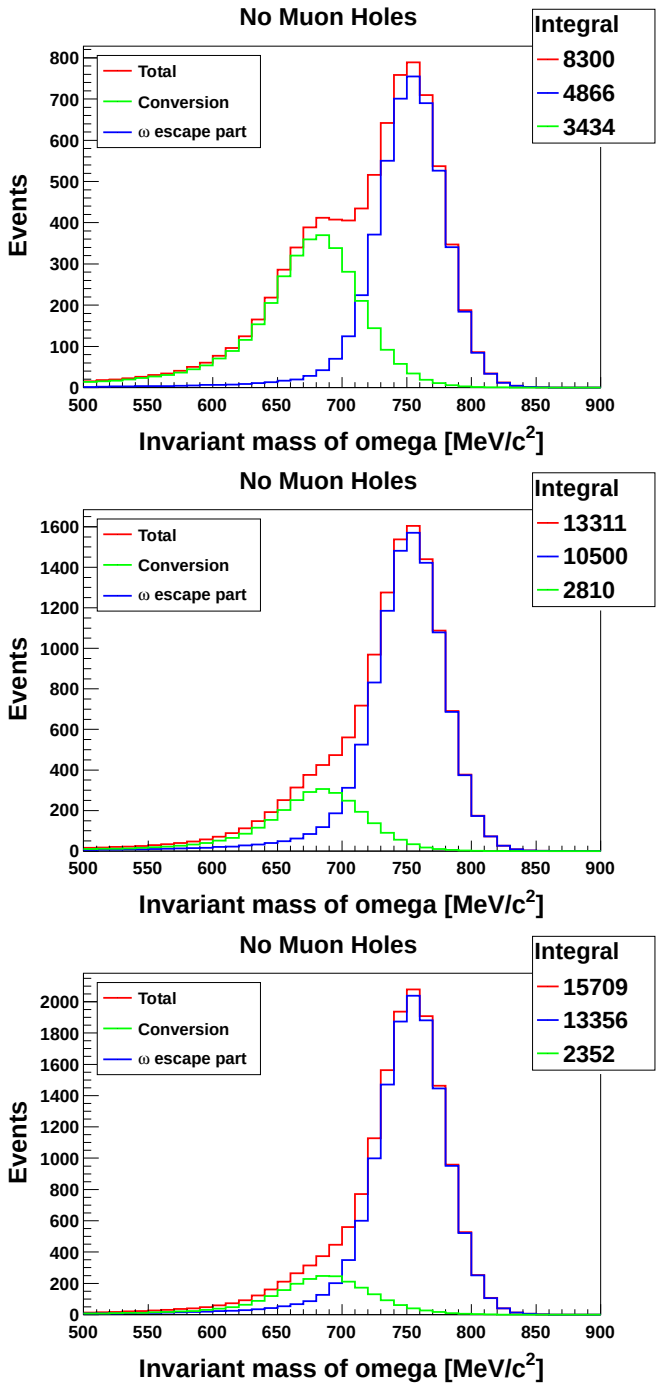

Figure 26: Expected invariant mass spectrum. Each panel shows calculated invariant mass distribution using assumed different potential. Green and blue lines represent conversion (mass modified) and escape (no modification) part, respectively.

Expected yields are summarized in Table 6.

Table 6: Summary of expected yields for Carbon

Potential	Total	ω escape part	Conversion (decayed inside nuclei)
(a)	8300	4866	3434
(b)	13311	10500	2810
(c)	15709	13356	2352

6.4 Expected missing mass spectrum

An expected missing mass spectrum of ω is shown in Fig.27. We assume that the neutron counter has 80ps time resolution and the neutron flight path is 7m in this evaluation. For this measurements, we don't need to require 3 γ's decay coincidence, so we use only neutron counter and more events can be expected.

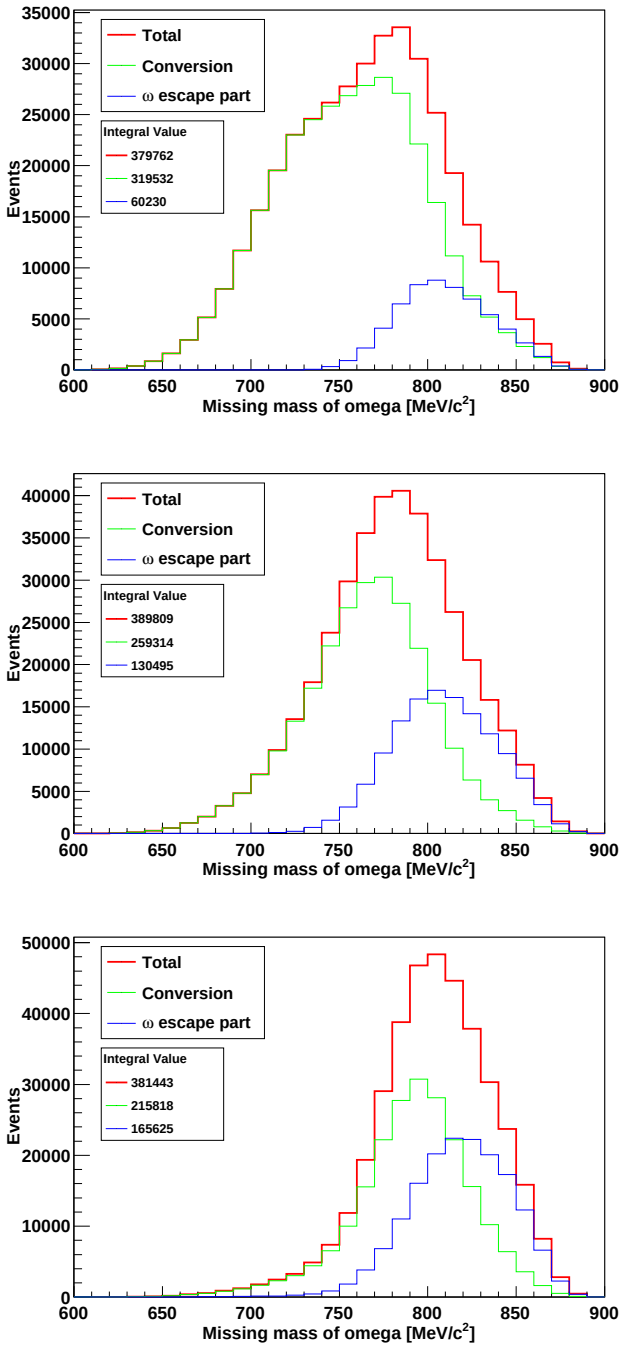

Figure 27: Expected missing mass spectrum without 3 γ's decay coincidence.

6.5 Final yield for physics

Estimated final yields for several targets are listed in Table 7. Yield of liquid hydrogen target is directly calculated from known cross section as shown in Fig.24. The cross section is 0.17 mb/sr in the Lab frame. Yield of Carbon is evaluated by the calculation described in the previous section. Yields of other targets are evaluated from results of Carbon. In the extrapolation, we assume $A^{2/3}$ dependence of ω cross section. Radiation loss of heavier targets are evaluated using target geometry.

Table 7: Final Yield

Target	thick-ness [cm]	density [g/cm^3]	Atomic Weight [g/mol]	radiation loss	Yield
For Atomic number dependence					
Liquid Hydrogen	6	0.071	2	0.99	2500
Carbon	6	2.267	12.01	0.89	8300
Calcium	6	1.55	40.08	0.75	3200
Niobium	0.3	8.57	92.91	0.85	2500
For combined measurements					
Carbon	6	2.267	12.01	0.89	8300
	events which has both forward neutron and ω decays				

7 Background estimation

The main background in final plot comes from p(π^-, n)$2\pi^0$ reactions. The background in 3 γ's measurements is 2 π^0 decays and 1 γ missing in the detection. The background in ω mass region is suppressed to 0.78 % of the originally produced $2\pi^0$. Combinatorial background is caused by non-correlated pairs and it can be subtracted using a mixed event method. To separate the signal from the background, the 1 γ missing background have to be understood well. This can be estimated with 4 γ events.

Estimated final spectra including background are shown in Fig.28.

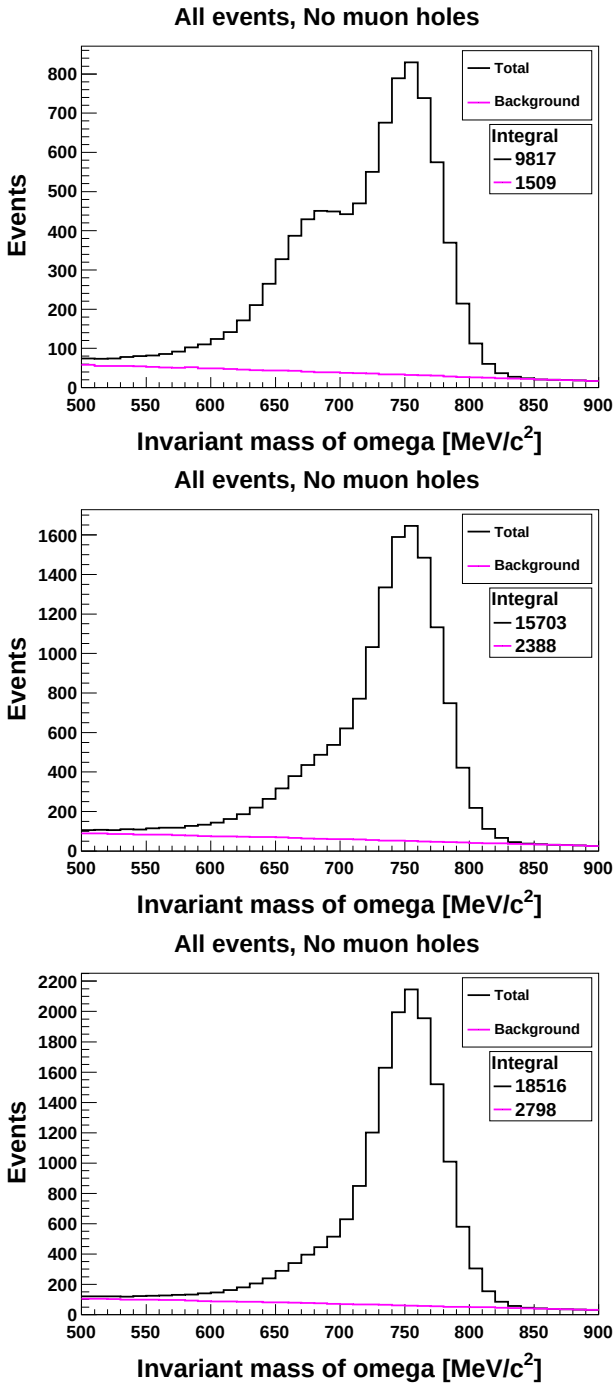

Figure 28: Final plot of invariant mass when the gamma-ray detector has no muon holes. The total events are shown in black lines, and the backgrounds are shown in magenta lines.

8 Final state interaction

Another issue is the final state interaction of π^0. It is evaluated for TAPS experiment using a transport model [23]. Fig.29 shows the calculation in [23]. According to this calculation, when π^0 meson is scattered in nucleus,

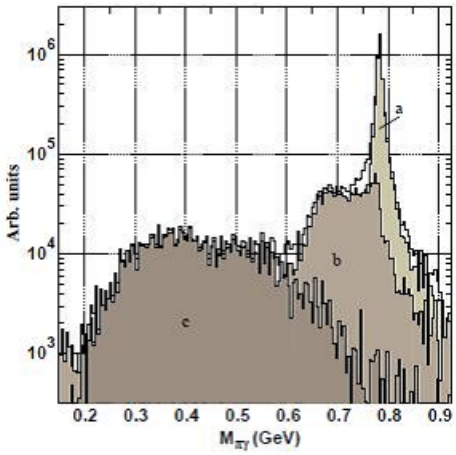

Figure 29: The $\pi^0\gamma$ mass distribution obtained from a Monte Carlo simulation of the process γ + Nb $\rightarrow \pi^0\gamma$ + X at E_γ = 1.2 GeV. The spectrum is decomposed into different contributions corresponding to the fraction of ω mesons decaying outside the nucleus (a), the fraction of ω mesons decaying inside for which the π^0 does not re-scatter (b), and the fraction of ω mesons decaying inside the nucleus for which π^0 re-scatters (c).

mass distribution of ω have very large shift in lower side, because π^0 meson scattering in nuclei is governed by δ dynamics and most of re-scattered π mesons have small kinetic energy (< 150 MeV). This situation doesn't change between γA and πA reactions [24]. Thus, the effect in interested mass region, i.e. just below ω mass, is negligible. However, 40% of ω mesons have the final state π^0 re-scattering in nucleus and final yield is decreased. The calculation is done for Niobium and gives an upper limit. Thus, we apply this number to all targets.

9 Trigger

Since we collect ω meson measured by a gamma detector, our main trigger is a coincidence of 3 γ's in the calorimeter and π^- beam. Geometrical matching and additional energy thresholds for γs are applied to select low momentum ω mesons. We prepared two sets of trigger condition to measure different mass and momentum region. Trigger 1 focus on large mass region ($500\mathrm{MeV}/c^2 < m_{\pi^0\gamma} < 850\mathrm{MeV}/c^2$) and low momentum ($p_{\pi^0\gamma} < 100\mathrm{MeV}/c$) to find a mass modification. Trigger 2 is for relatively small mass region ($710\mathrm{MeV}/c^2 < m_{\pi^0\gamma} < 850\mathrm{MeV}/c^2$) and higher momentum ($p_{\pi^0\gamma} < 400\mathrm{MeV}/c$) to measure a atomic number dependence of ω cross section. Both triggers require that there is no additional γ which has an energy larger than 20 MeV.

The trigger scheme is following.

1. Find a crystal hit which has an energy in the specified range ($\mathrm{p}_{\gamma 1}$).
2. Search another hit ($\mathrm{p}_{\gamma 2}$) in corresponding geometrical position($\theta_{\gamma_1\gamma_2}$).
3. Require another hit which has an energy larger than 20MeV ($\mathrm{p}_{\gamma 3}$).
4. Veto the event, if there is an additional (4th) γ hit which has an energy larger than 20MeV.

Table 8 shows configuration, efficiency, and rejection factor for $2\pi^0$ of the trigger.

Table 8: Trigger configuration

Trigger Name	Trigger scheme	Efficiency for ω	Rejection factor for $2\pi^0$
Trigger 1	$200 \leq p_{\gamma 1} \leq 470$MeV, $120 \leq p_{\gamma 2} \leq 420$MeV, $20\mathrm{MeV} \leq p_{\gamma 3}$, $2.4\mathrm{rad} \leq \theta_{\gamma_1\gamma_2}$	96.1%	125
Trigger 2	$280 \leq p_{\gamma 1} \leq 660$MeV, $120 \leq p_{\gamma 2} \leq 480$MeV, $20\mathrm{MeV} \leq p_{\gamma 3}$, $2.0\mathrm{rad} \leq \theta_{\gamma_1\gamma_2}$	95.5%	46

Figure 30 shows trigger efficiency as a function of mass for several momentum of ω meson. The trigger configurations achieve a flat response for objective mass and momentum range.

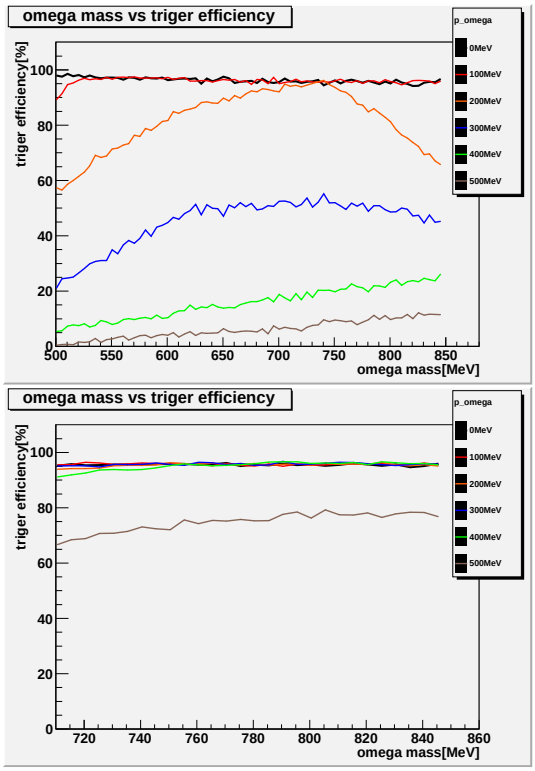

Figure 30: Trigger bias on mass for Trigger 1(Top) and Trigger 2(Bottom).

Thus, main background at the trigger is p(π^-, n)$2\pi^0$ reaction and 1γ missing. Total trigger rate is dominated by the background and estimated by existing data. Fig.31 shows measured total cross section for the reactions $\pi^- p \to X$. Finally, the main trigger rate becomes 2k events per spill. The calculation assume isotropic angular distribution. The angular distribution is measured at slightly lower beam momentum [25] and it shows forward peaking distribution. Thus, trigger rate can be decreasing, since low momentum mesons is generated in backward region.

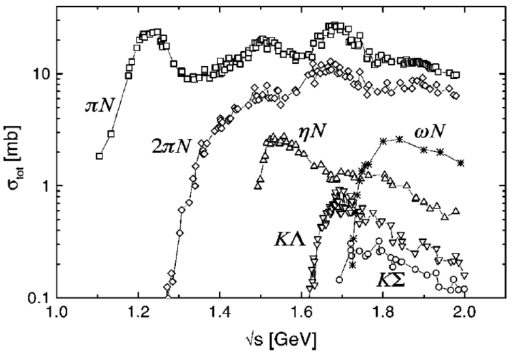

Figure 31: Total cross sections for the reactions $\pi^- p \to X$ with X as given in the figure [22].

In addition to the main trigger, we have several triggers for additional physics and calibrations. We have additional trigger which requires π^- beam and forward neutron hit to search ω bound states. To measure ω bound states, information of ω decays is not necessary, however, forward neutron measurements will have a huge background without ω decays information. For example, an experiment performed at BNL to search η bound state shows a continuum background of 0.1 mb /sr/MeV [26]. Then, the trigger rate will become $10 \sim 100$ times larger than the main trigger and need to be prescaled to match DAQ band width. The trigger is used to evaluate a trigger bias of the main triggers.

Also, we have two γs detection trigger for calibration purpose to select π^0 events. With the trigger, high momentum ω mesons can be detected also and such ω mesons don't have a nuclear medium effect, since almost ω mesons are decayed outside nucleus. Experimental effects, such as shower leakage tails, can be checked with this trigger data.

For combined measurements, we will have a coincidence of neutron trigger and two γs trigger.

10 Combined measurements

Figure 32, Figure 33 and Figure 34 show correlation plots between invariant mass and missing energy. Left top figures are without smearing. Left bottom figures are smeared by resolution of gamma-ray detector. Right top figures are smeared by time resolution of neutron counter. Right bottom figures are smeared by both detectors. Invariant mass spectra which calculated by this model are shown in 35. Applying a cut of $E_\omega < E_0$, the mass shifted part can be selected and the spectrum can be decomposed two parts, such as bound region (green) and no-bound region (blue). The total spectrum is shown as a red line.

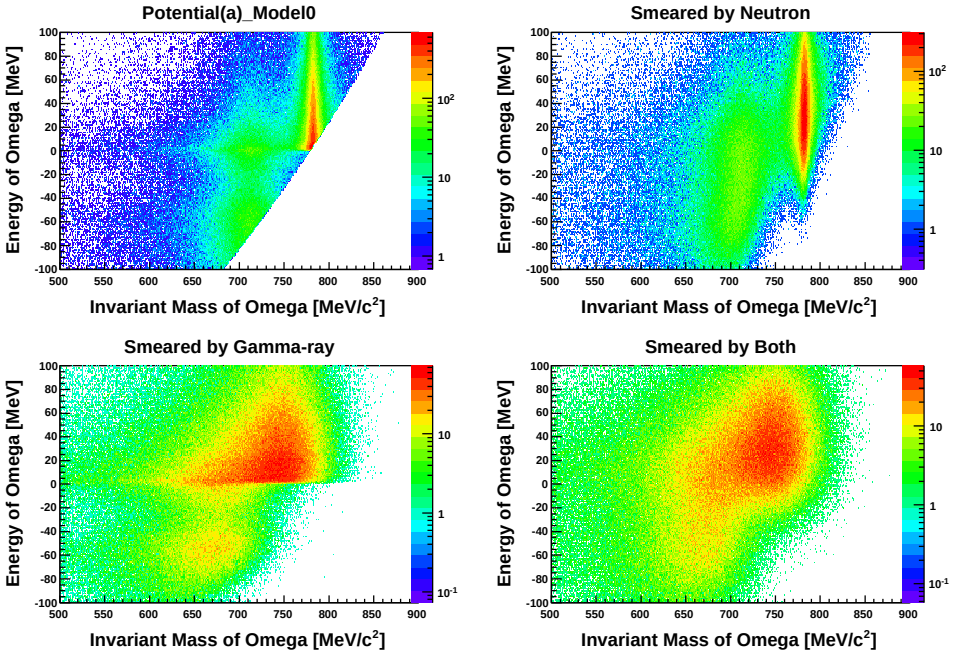

Figure 32: Correlation plots between invariant mass and missing energy.

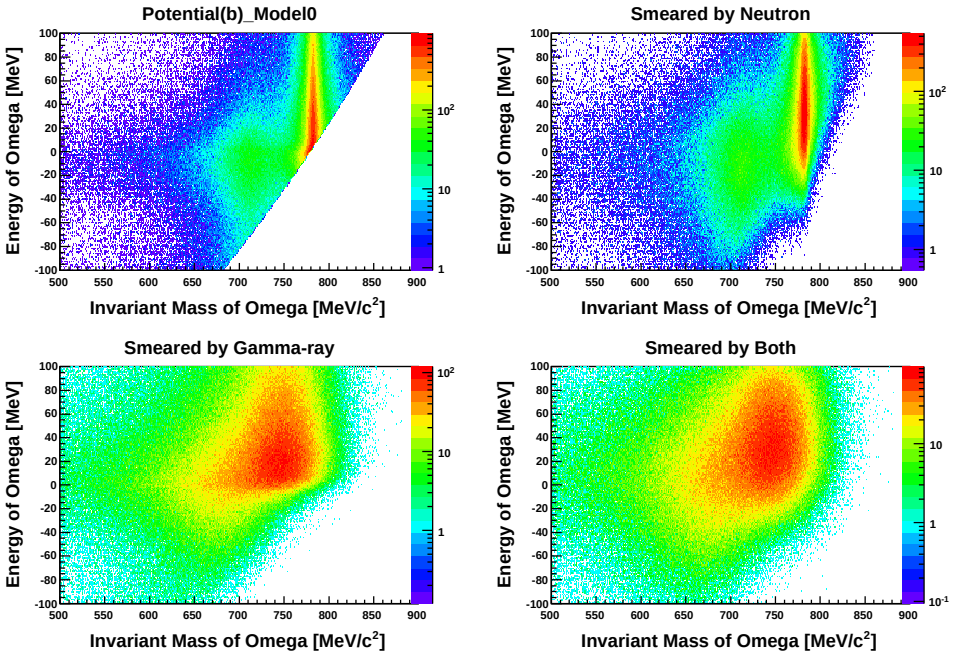

Figure 33: Correlation plots between invariant mass and missing energy.

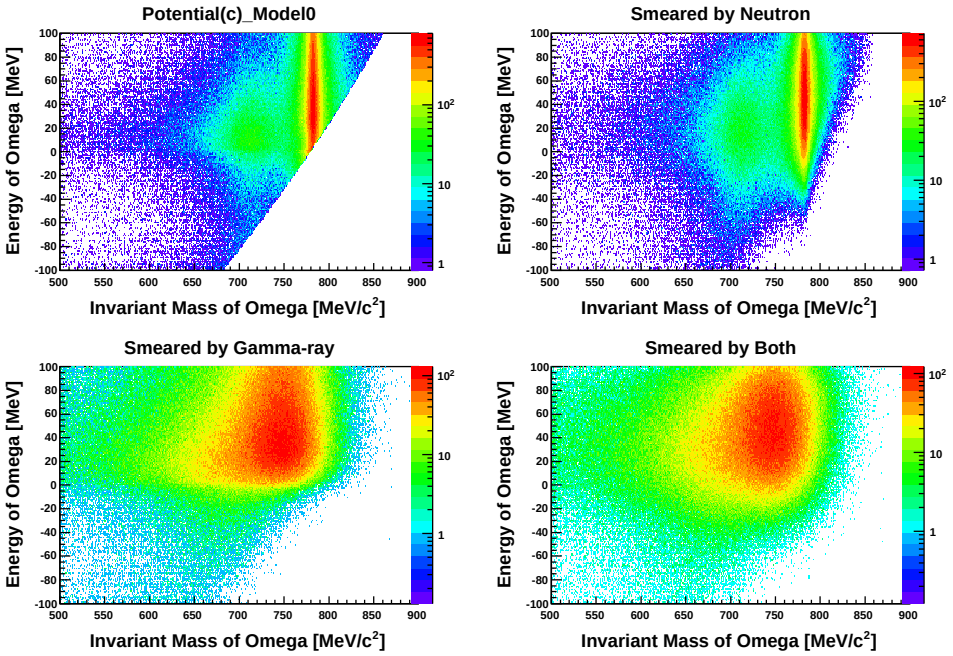

Figure 34: Correlation plots between invariant mass and missing energy.

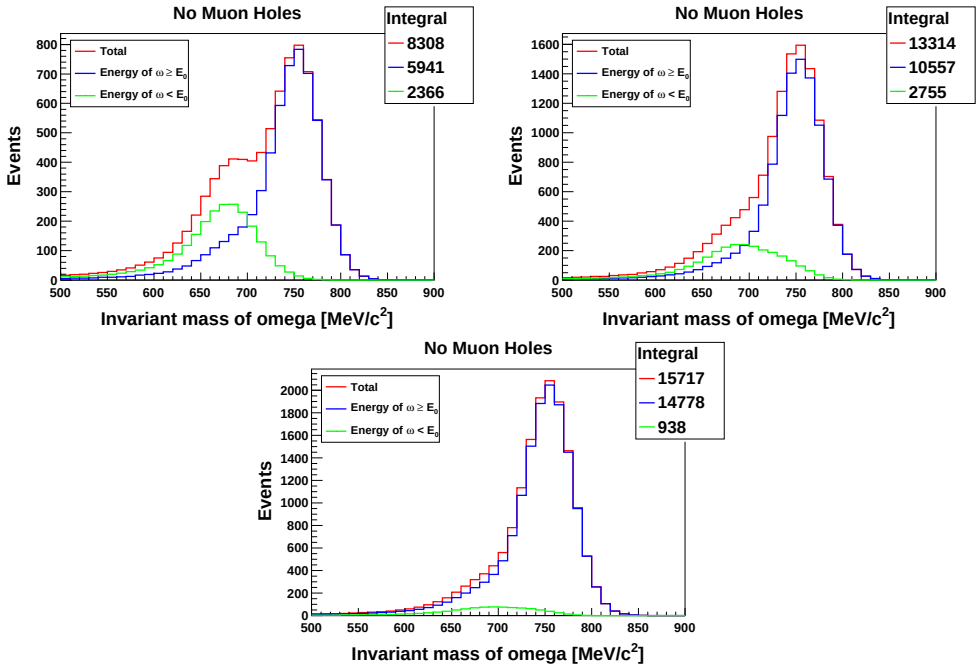

Figure 35: Expected invariant mass spectrum for potentials

Figure 36, Figure 37 and Figure 38 represent correlation plots of another model. In this model, we assume a strong correlation between invariant mass and missing mass. Invariant mass spectra which calculated by this model are shown in Fig. 39.

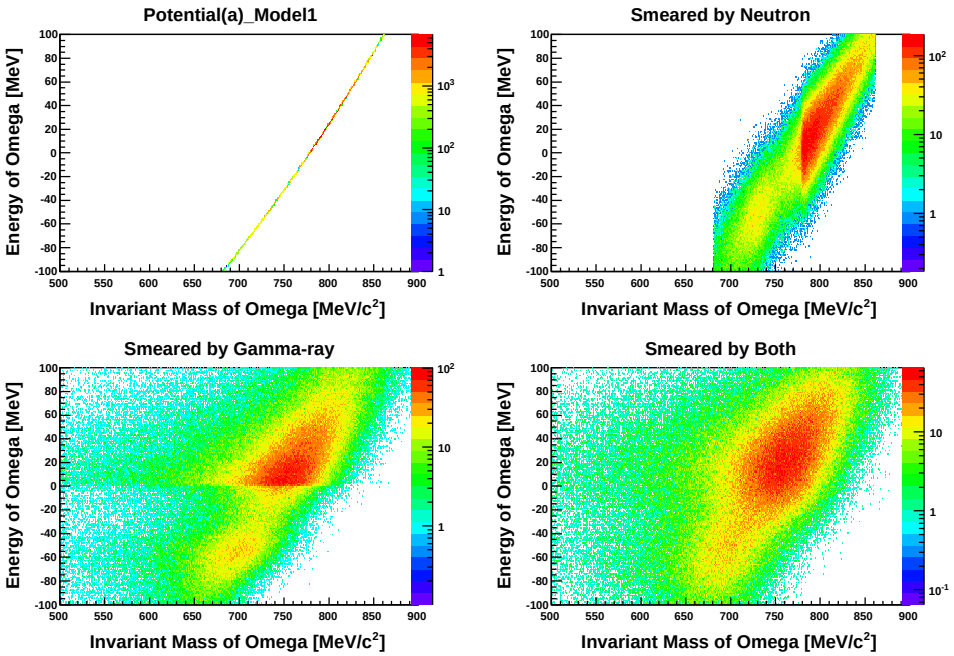

Figure 36: Correlation plots between invariant mass and missing energy.

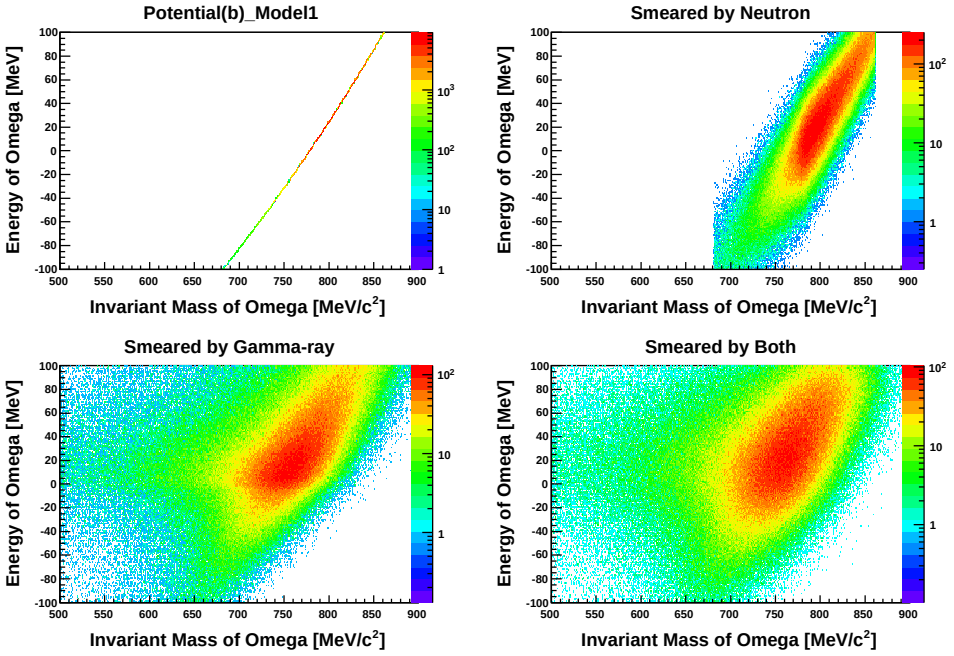

Figure 37: Correlation plots between invariant mass and missing energy.

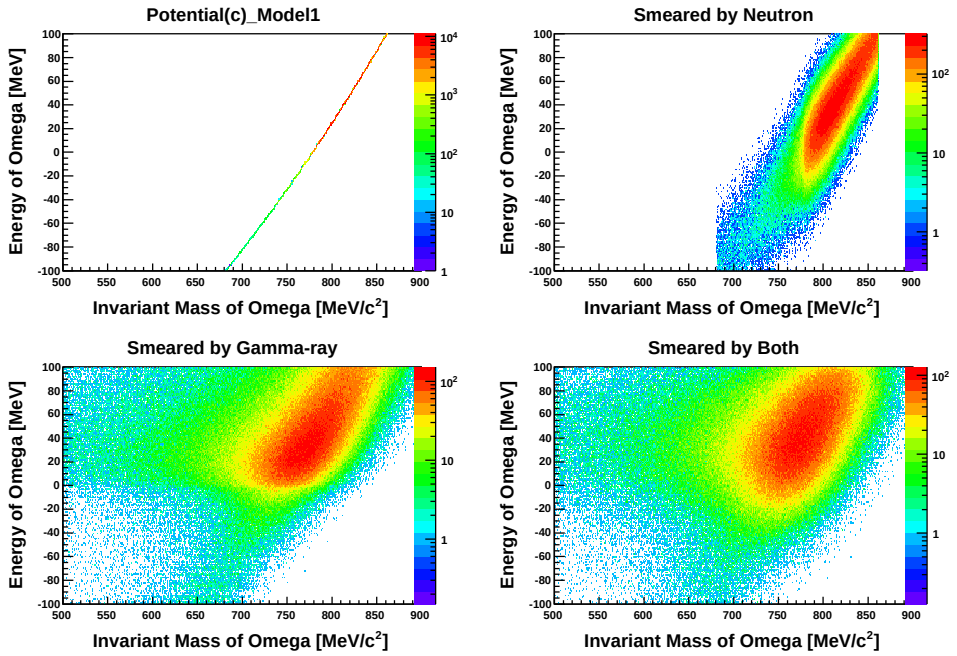

Figure 38: Correlation plots between invariant mass and missing energy.

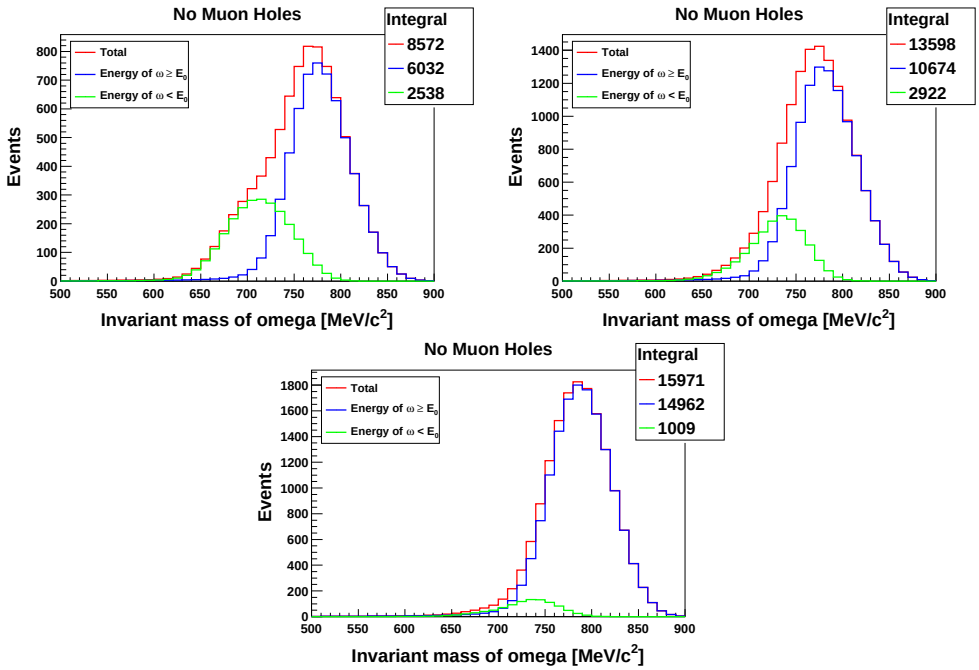

Figure 39: Expected invariant mass spectrum for potentials

11 Cost estimation

A brief cost estimation is shown in Table 9.

Table 9: cost estimation

Detector	element	description	Budget	cost [M Yen]
Beam Line	Tracker	MWPC	Common use	0
	Start Counter	Segmented scintillator	Common use	0
Neutron	Frame		Grant(Kakenhi)	1
Counter	PMT	48 x H2431	Grant(Kakenhi)	10
	Scintillator	24 pieces	Grant(Kakenhi)	2
EM		Reuse of E06 CsI(Tl) or Tohoku BGO		0
Calorimeter				
	Additional Crystals	Fill Muon hole	Grant submitted	48
	Avalanche Photo Diode	For Additional Crystal	Grant submitted	11
	Readout Circuit	For Additional Crystal	Grant submitted	4
	Frame		Grant submitted	3
Total				81

12 Summary

We propose measurements of ω mass modification in nucleus using $\pi^0\gamma$ decay mode. To investigate the mass modification in nucleus, measurement of cross section and mass distribution as a function of atomic number using several target. The measurements focus on slowly moving ω mesons to maximize nuclear matter effects. In addition, combined measurements of nuclear ω bound state and direct ω mass modification is performed. Nuclear ω bound states are measured in A(π^-, n)ω reaction. Such exclusive measurement can supply essential information to establish mass modification of vector mesons in nucleus.

References

[1] T. Hatsuda and S.H. Lee, Phys. Rev. **C46** (1992) R34.

[2] T. Hatsuda and T. Kunihiro, Phys. Rep. **247** (1994) 221.
G.E. Brown and M. Rho, Phys. Rep. **269** (1996) 333.
W. Cassing and E.L. Bratkovskaya, Phys. Rep. **308** (1999) 65.

[3] F. Klingl, N. Kaiser and W. Weise, Nucl. Phys. **A624** (1997) 527.
F. Klingl, N. Waas and W. Weise, Nucl. Phys. **A650** (1999) 299.

[4] M.F.M. Lutz, Gy. Wolf and B. Friman, Nucl. Phys. **A706** (2002) 431.

[5] P. Muehlich *et al.* , Nucl. Phys. **A780** (2006) 187.

[6] F. Sakuma *et al.* , Phys. Rev. Lett. **98** (2007) 152302.

[7] D. Trnka *et al.* , Phys. Rev. Lett. **94** (2005) 192303.

[8] M. Kaskulov *et al.* , Phys. Rev. **C75** (2007) 064616.

[9] E. Marco and W. Weise, Phys. Lett **B502** (2001) 59.

[10] H. Nagahiro, D. Jido, and S. Hirenzaki, Nucl. Phys. **A761** (2005) 92.
H. Nagahiro, D. Jido, S. Hirenzaki, e-Print: arXiv:0811.4516 [nucl-th].
H. Nagahiro, private communication.

[11] K. Ozawa *et al.* , Phys. Rev. Lett **86** (2001) 5019.
M. Naruki *et al.* , Phys. Rev. Lett **96** (2006) 092301.
R. Muto *et al.* , Phys. Rev. Lett **98** (2007) 042501.

[12] C. Djalali *et al.* , J. Phys. **G34** (2007) S495.

[13] M. Nanova *et al.* , arXiv:1005.5694 V. Metag *et al.* , JPS-DNP at Hawaii presentation

[14] P. Muhlich *et al.* , Eur. Phys. J. A **20** (2004) 499. P. Muhlich, PhD thesis, Univ. of Giessen, (2006)

[15] K. Gallmeister *et al.* , Prog. Part. Nucl. Phys. **61** (2008) 283.

[16] M. Kotulla *et al.* , Phys. Rev. Lett **100** (2008) 192302.

[17] M. Kaskulov, Eur. Phys. J. A **31** (2007) 245.

[18] D.V. Dementyev *et al.* , Nucl. Instrum. Meth. **A440** (2000) 151.

[19] Yu.G. Kudenko, Nucl. Instrum. Meth. **A494** (2002) 318.

[20] T. Ishikawa, privae communication.

[21] J. Keyne *et al.* , Phys. Rev. **D14** (1976) 28.

[22] G. Penner and U. Mosel, Phys. Rev. **C65** (2002) 055202.

[23] J.G. Messchendorp, A. Sibirtsev, W. Cassing, V. Metag, and S. Schandmand, Eur. Phys. J. **A11**, 95-103 (2001))

[24] V. Metag, private communication

[25] S. Prakhov *et al.* , Phys. Rev. **C69** (2004) 045202.

[26] R.E. Chrien *et al.* , Phys. Rev. Lett. **60** (1988) 2595.